33RD CONGRESS
OF THE INTERNATIONAL COUNCIL
OF THE AERONAUTICAL SCIENCES
STOCKHOLM, SWEDEN, 4-9 SEPTEMBER, 2022

ICAS 2022 SWEDEN

COUPLED AEROPROPULSIVE ANALYSIS AND OPTIMIZATION OF A HIGH BYPASS TURBOFAN ENGINE

Andrew H. R. Lamkin[1], Anil Yildirim[2] & Joaquim R. R. A. Martins[3]

[1]Ph.D. Candidate, Department of Aerospace Engineering, University of Michigan
[2]Postdoctoral Research Fellow, Department of Aerospace Engineering, University of Michigan
[3]Professor, Department of Aerospace Engineering, University of Michigan

Abstract

Advances in aeropropulsive design optimization provide new capabilities for the study of tightly integrated propulsion systems. New techniques that couple CFD solvers to thermodynamic cycle analyses showed increased robustness and proved the viability of a fully coupled approach using gradient-based optimization. However, existing work in this area has been limited to simple benchmark cases and does not contain complete engine models. In this study, we extend these methodologies beyond an electrically driven propulsor to consider a complete high-bypass turbofan engine. The high-bypass turbofan model incorporates CFD and thermodynamic cycle sub-systems into a unified model for aeropropulsive design optimization by utilizing multiple coupling techniques from prior benchmark aeropropulsive cases. We present a high-bypass turbofan design optimized for thrust specific fuel consumption with respect to coupling, geometric, and practical design constraints using this coupled approach. The integration of high-fidelity aerodynamic shape optimization with one-dimensional cycle modeling on a large scale is a major milestone for coupled propulsion system design. These developments advance the use of coupled aeropropulsive optimization earlier in the design cycle for propulsion systems.

Keywords: Optimization, Aeropropulsive, Multidisciplinary, Turbofan

1. Introduction

Models used for propulsion system design often fail to capture the complex interactions between aerodynamics, thermodynamics, and the nacelle geometry. These include zero and one-dimensional cycle models, which are common techniques for engine analysis that use first principles approaches and simplifying assumptions. The strength of these methods comes from turbomachinery maps and detailed thermodynamic calculations that accurately approximate physical processes that are otherwise computationally challenging to model in high fidelity. These methods extract enough information about the underlying thermodynamics to make moderately informed design decisions, but higher dimensionality effects from the flow field and most geometric degrees of freedom are neglected.

Coupled aeropropulsive models can be used for including higher-order effects in the design of propulsion systems, in which one-dimensional cycle analyses are coupled to higher-fidelity aerodynamic solvers and geometry kernels. Lytle [1] proposed using the Numerical Propulsion System Simulation (NPSS) library [2] to couple zero-dimensional cycle analyses with one-dimensional meanline tools and three-dimensional computational fluid dynamics (CFD). This multi-fidelity capability, referred to as “zooming”, provides a method for modeling propulsion components in varying levels of fidelity and loosely coupling them at joint interfaces. Although introducing necessary multi-fidelity concepts, zooming lacks three-dimensional geometric coupling and does not consider the aerodynamics of the nacelle or bypass. Additionally, the NPSS library does not compute the derivatives necessary for gradient based design optimization.

In fact, research on coupled aeropropulsive design optimization is scarce. Gray et al. [3] and Yildirim et al. [4] summarize the limited literature on engine nacelle optimization and the challenges of integrating the required disciplines in a design framework. Several studies used gradient-free algorithms to optimize the nacelle design or the nacelle-wing integration [5–14], but they lacked multidisciplinary models and were limited by the possible number of design variables that could be used [15].

Briones et al. [16] presented one of the first examples of fully coupled aeropropulsive analysis, but until recently, no framework enabled gradient-based design optimization using coupled aeropropulsive models. Gray et al. [3] and Yildirim et al. [4] proposed a new benchmark aeropropulsive model of a simple podded electric propulsor that uses a podded fan model built with pyCycle [17], a one-dimensional cycle modeling library with analytical gradients; and an aerodynamic model with ADflow [18], a Reynolds-averaged Navier–Stokes (RANS) CFD solver that uses structured multi-block and overset meshes. The aerodynamic and propulsion models are coupled with MPhys[1], a multiphysics library built using OpenMDAO [19] for gradient-based design optimization. Yildirim et al. used this coupled model to develop two different coupling techniques, namely the actuator zone (AZ) and boundary condition (BC) versions, to transfer information between pyCycle and ADflow. The AZ coupling strategy introduces momentum and energy source terms to represent the impact of the propulsion system on the flow field [20, 21]. The BC approach, on the other hand, passes the mass, momentum, and energy outputs to the optimizer as constraints and allows the optimizer to balance the residuals between the propulsion cycle and flow field. They demonstrated the capabilities of these coupled models by performing a range of design optimizations [4]. However, these studies were limited to a simple podded electric fan and did not include a complete engine model.

In this work, we extend the capability of this existing aeropropulsive design framework to a high-bypass turbofan (HBTF) model by incorporating a turbojet core within the nacelle of a podded propulsor. The HBTF model takes advantage of OpenMDAO's modularity by separating the fan and core into separate pyCycle models, coupled together by a mechanical low pressure shaft. The AZ coupling method is then applied to the fan, and the BC method is applied to the core. Unlike previous studies, we include a turbojet core and use one-dimensional meanline analysis to vary the flow paths, turbomachinery, and thermodynamics. We model the fan in pyCycle and feed back heat information to ADflow to complete the AZ coupling loop. All other flow paths are modeled using RANS CFD, including the inlet, bypass duct, and nozzles.

This study demonstrates the utility of mixed-fidelity methods in the design of large-scale propulsion systems. We present a new optimization problem that combines the AZ and BC coupling strategies with conventional design knowledge derived from zero and one-dimensional propulsion cycle simulations. Furthermore, our approach captures the high-order interactions between the nacelle aerodynamics and the propulsion system. This is a significant step forward toward large-scale and high-fidelity gradient-based optimization of aircraft propulsion systems in the preliminary design stage.

The remainder of this paper is structured as follows. Sec. 2.describes the coupled aeropropulsive modeling approach and the design framework structure. In Sec. 3.we lay out the optimization problem and in Sec. 4.we present the results from the analysis and optimizations. Finally, we present the conclusions in Sec. 5.

2. Methodology

In this section, we detail the coupled aeropropulsive design framework we developed based on the two aeropropulsive coupling approaches introduced by Yildirim et al. [4]. Combining these approaches to model complete turbofan configurations necessitates the use of multiple coupling and mixed-fidelity strategies. Unlike the podded fan, the turbofan MDA model we introduce in this work includes two separate pyCycle subsystems for the fan and the core. We use the AZ coupling strategy for the fan and the BC method for the core, which results in both pyCycle subsystems being fully coupled to the CFD model.

For clarity, we use standardized flow station numbering and component naming scheme shown in Fig. 1 to refer to locations and elements along the turbofan flow path. Furthermore, we extend these conventions to the core thermodynamic cycle, as shown in Fig. 7. The core cycle begins at station

[1] https://github.com/OpenMDAO/mphys

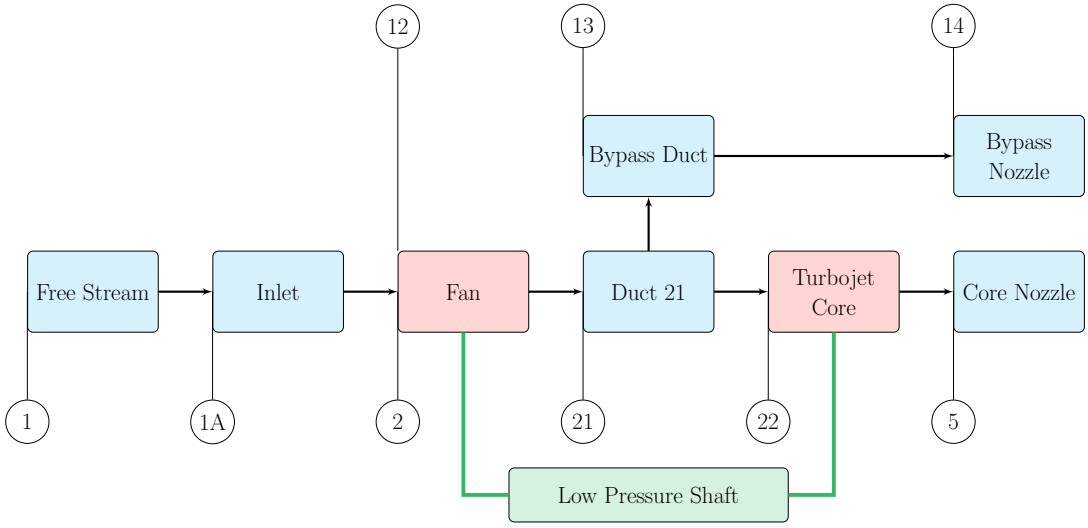

Figure 1 – Top level flow station numbering and component labels for the high-bypass turbofan model. Aerodynamic model elements are shown in blue and one-dimensional cycle models are shown in red. Green lines and elements represent mechanical connections and elements. The black arrows show the direction of the flow through the engine.

22 with the low pressure compressor (LPC) and ends at station 42 with the low pressure turbine (LPT). An extended design structure matrix (XDSM) [22] of the complete MDA model is shown in Fig. 2. In the following sections, we detail each computational component in the aeropropulsive design framework.

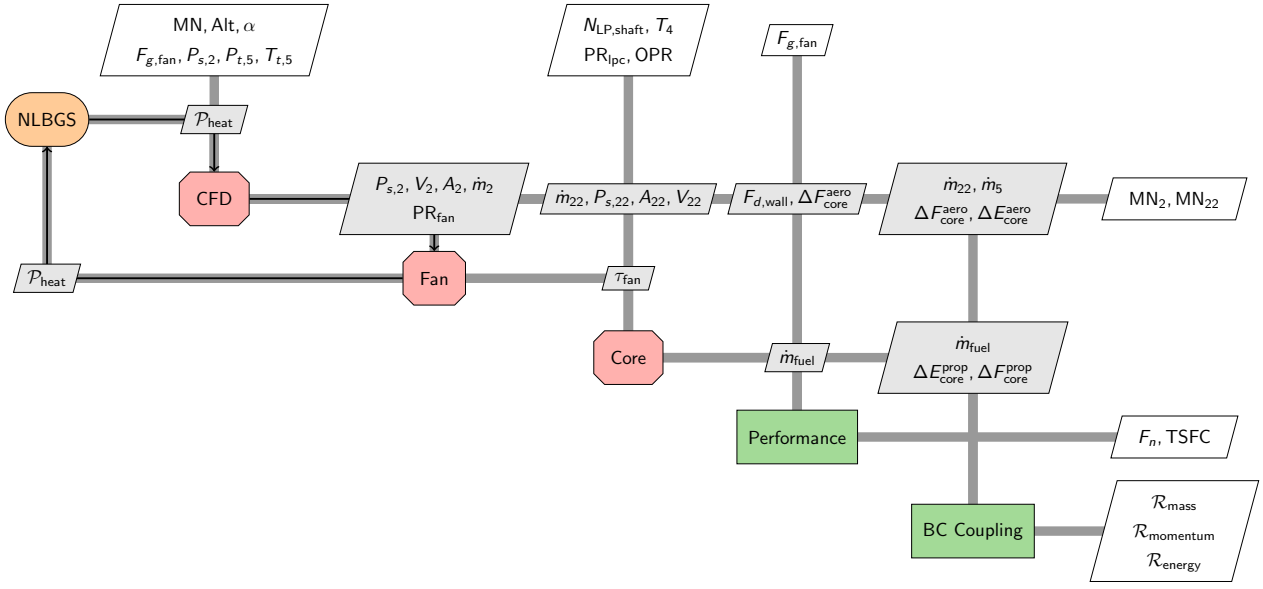

Figure 2 – XDSM of the fully coupled MDA model. Vertical lines represent inputs to the components, whereas horizontal lines are outputs. The black arrows detail the NLBGS solver loop for the AZ coupling. Red octagons are implicit groups that contain nested nonlinear solvers, and green rectangles are explicit functions. The outputs on the right hand side are passed to the optimization problem as the objective function or constraints.

2.1 Geometry Parametrization and Mesh Deformation

We use OpenVSP [23] for the geometry parameterization, which is a parametric geometry tool that uses Bézier curves and surfaces to represent geometric components. The baseline geometry is

derived from a cross sectional drawing of a Pratt and Whitney 1500G series turbofan found in the book “Jet Propulsion” by Cumpsty and Heyes [24]. We created four components in OpenVSP that represent the nacelle, spinner, core nacelle, and core plug. Figure 3 provides an isometric view of each OpenVSP engine component and the full configuration with all components shown.

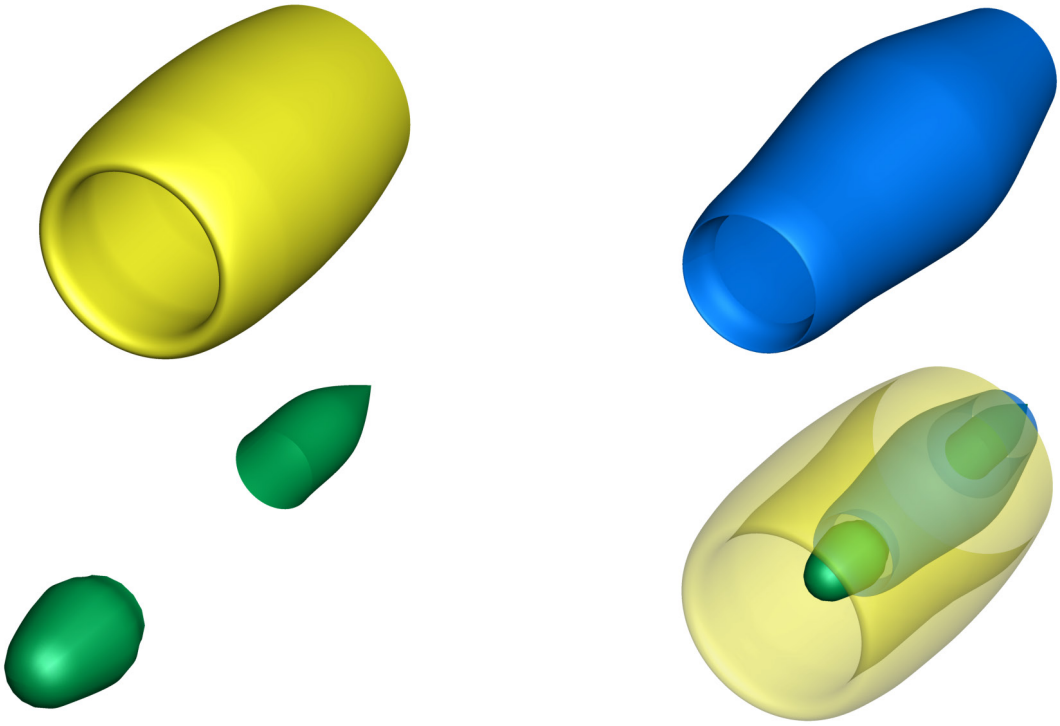

Figure 3 – An isometric view of the four geometric components modeled in OpenVSP. The nacelle is in the upper left, core in the upper right, spinner and core plug in the lower left, and the full geometry configuration is in the lower right corner.

Each component is defined by the cross sections and tangent angles required to generate the underlying Bézier surfaces. The nacelle has 14 cross sections with 4 on the outer nacelle, 8 on the inner nacelle, 1 on the leading edge, and 2 on the trailing edge. All cross sections that make up the inner and outer portions of the inlet are elliptical, with both height and width degrees of freedom to account for potential off-design cases that consider cross-flow. The remaining nacelle cross sections, including three that comprise the fan disk, are circular. Cross-flow is less prominent aft of the fan, hence we designed the spinner, core, and core plug with solely circular cross sections.

For this study, we consider the cross section diameters, widths, and heights as design variables, but omit the tangent angles for simplicity. Some groups of cross sectional diameters are linked to preserve geometric features such as the fan disk diameter, duct shape, or constant trailing edge thickness. In particular, the cross section diameters that comprise duct 21 are linked with a constant offset to preserve the s-duct profile. Furthermore, we do not add any spinner cross sections to simplify the inlet, fan, bypass, and duct 21 integration.

Multiple arrays of “toothpick” constraints are added to the nacelle and the core wall between duct 5 and the bypass stream. These constraints ensure that the thickness of certain sections cannot be less than the baseline or more than three times the baseline thickness. Toothpick constraints take the place of structural considerations that we do not include in this work. Figure 4 shows the toothpick constraint locations along the nacelle and core geometries.

We leverage the methods developed by Yildirim et al. [25, 26] for using OpenVSP with CFD-based design optimization. At each design iteration, OpenVSP is used to generate an updated surface that we use to update the CFD volume mesh using the mesh deformation algorithm by Luke et al. [27]. We use the the open-source mesh deformation library IDWarp developed by Secco et al. [28] to perform the mesh deformation step shown in Fig. 8. The optimizer passes updated shape design variables to the geometry element, which then calculates the surface mesh node positions and transfers them to

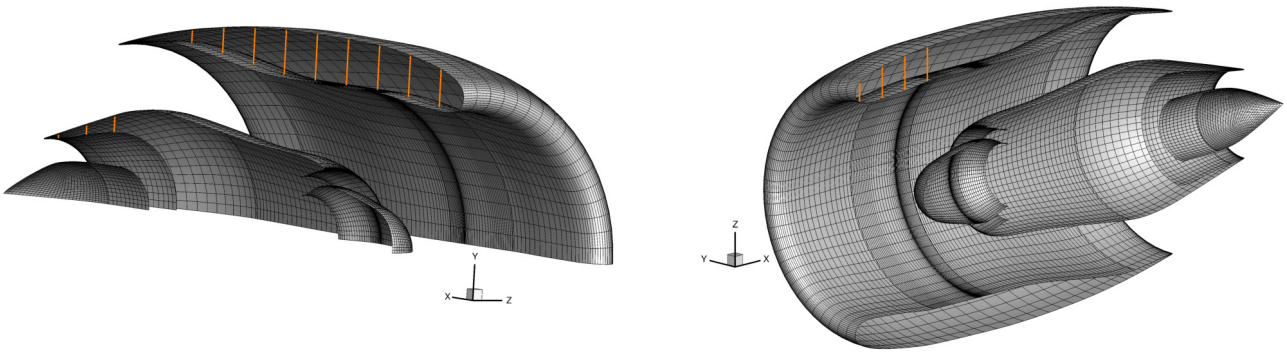

Figure 4 – Geometric thickness constraints for the nacelle and duct5 walls. The left figure shows the axisymmetric thickness constraints and the right figure shows the thickness constraints for the elliptical cross sections forward of the fan disk.

IDWarp. After mesh deformation, the new volume mesh is used by the aerodynamic model to perform CFD analysis.

2.2 Aerodynamic Model

We use the open-source CFD solver ADflow [18] for aerodynamic analyses, which solves the RANS equations on structured multi-block and overset meshes using a finite volume scheme. To compute the flow field in and around the turbofan geometry, we employ the Spalart–Allmaras (SA) turbulence model [29] in conjunction with RANS simulations. ADflow offers advantages for aeropropulsive design optimization, including an efficient adjoint solver to compute analytic derivatives [30], a Python interface to couple it to a larger aeropropulsive design framework [18], and an approximate Newton-Krylov solver to handle the challenging flow simulations that arise from the use of body force terms and powered boundary conditions [31].

The mixed AZ and BC coupling strategy in this work introduces unique challenges related to mesh generation, solver robustness, and problem formulation. We created the three-dimensional half-body mesh, shown in Fig. 5, using distinct overset regions that each satisfied requirements of the aerodynamic model. First and most important, the fan disk is an axi-symmetrical overset block that encapsulates the actuator region without overlap from neighboring overset meshes. This is critical because the AZ coupling method distributes energy and momentum source terms to all cells within the AZ [32].

Next, the bypass duct, duct21, and duct5 are internal volume blocks with sufficient resolution dependent on the size of the accompanying geometric feature. Third, we generated structured surface meshes for the spinner and core plug, which are then extruded to obtain volume meshes using the pyHyp library [28], an open-source hyperbolic volume mesh marching tool. The nacelle, splitter, and bypass nozzle surface meshes add necessary resolution at trailing and leading edges of the nacelle and core geometry. We extrude these surface meshes to volume meshes using pyHyp [28], which completes the full set of overset meshes for the aerodynamic model. Finally, we include a background cartesian mesh that is extruded to far-field boundary conditions. The current mesh contains 1.3 million cells, which is adequate to capture the main flow features around the different flow streams of the fan for aeropropulsive design optimization.

Yildirim et al. [4] used a three-dimensional control volume drawn around the cells inside the AZ to calculate the total energy added to the flow due to the momentum source terms as

$$\mathscr{P}_{\text{flow}} = \iiint_{\text{AZ}} \left(\vec{V} \cdot \vec{f} \right) dv. \tag{1}$$

The terms $\vec{V}$ and $\vec{f}$ are the local velocity and total force inside each CFD volume cell. Additionally, the total flow power includes the heat added to flow by non-adiabatic losses in the fan [32]. The total AZ power is

$$\mathscr{P}_{\text{total}} = \mathscr{P}_{\text{flow}} + \mathscr{P}_{\text{heat}}. \tag{2}$$

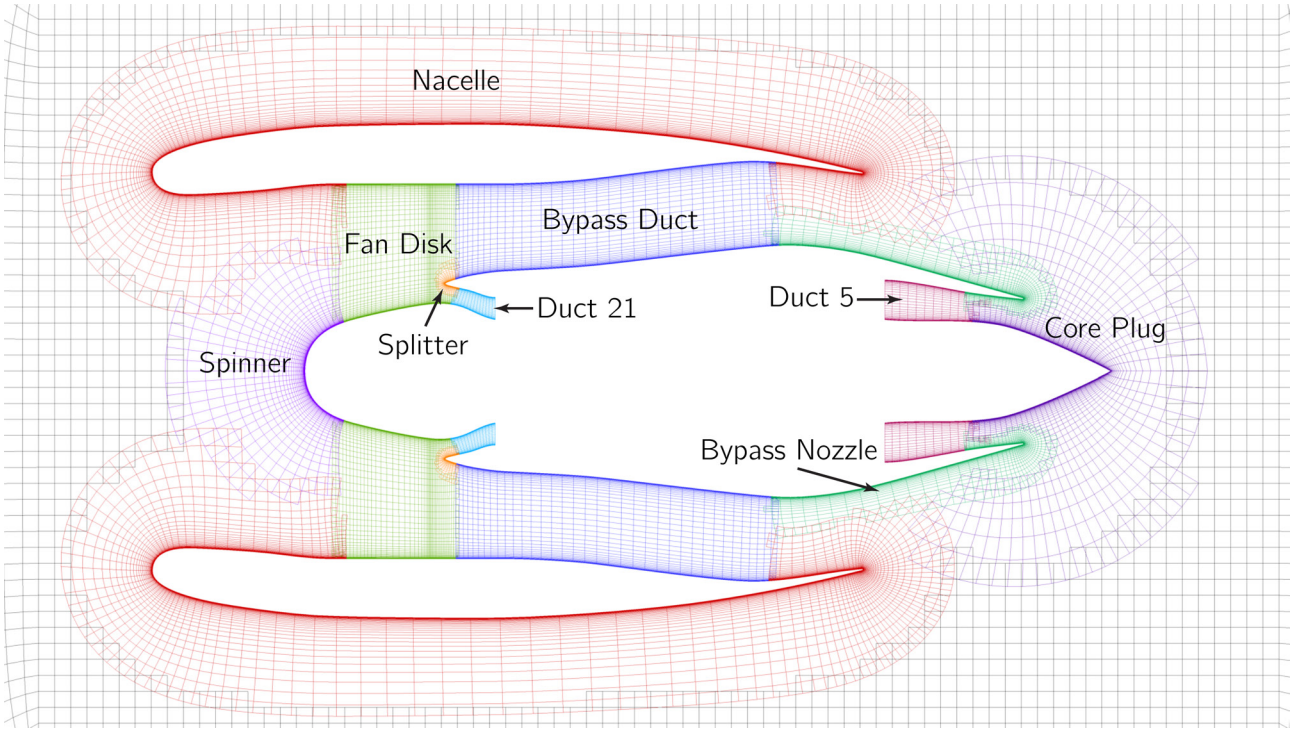

Figure 5 – Overset mesh regions for the aerodynamic model. Each color corresponds to a mesh region generated as a standalone volume block or an extruded surface mesh. We only show the cells on the symmetry plane in this figure.

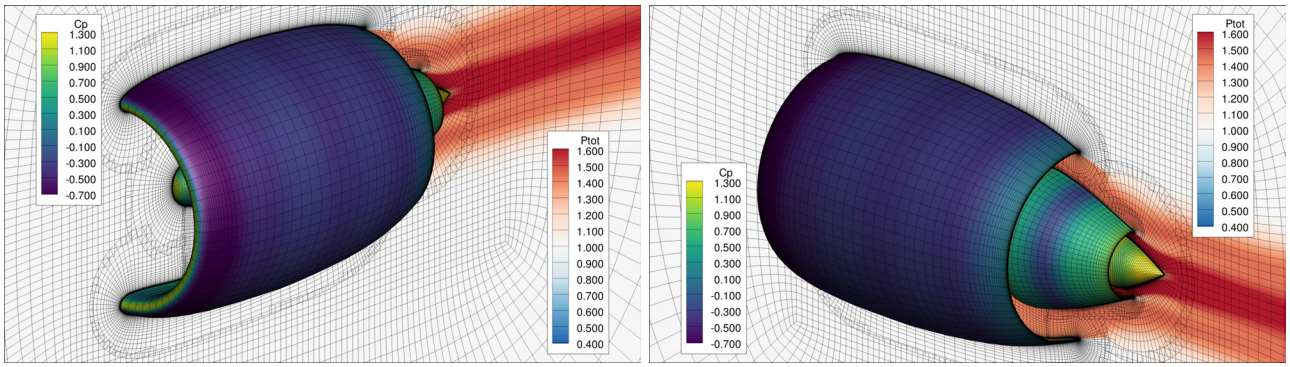

Figure 6 – Isometric view of the feasible solution to the aeropropulsive optimization problem outlined in sec. 3. Pressure coefficient contours are displayed on the nacelle, core nacelle, spinner, and plug. Total pressure contours are shown along the symmetry plane.

The BC coupling needs the change in mass, momentum, and energy across the core for the conservation residuals. The momentum change is the difference between the integrated pressure and momentum forces at flow station 5 and 22, computed as

$$\Delta F_{\text{core}}^{\text{aero}} = \left(F_{5,\text{momentum}}^{\text{aero}} + F_{5,\text{pressure}}^{\text{aero}}\right) - \left(F_{22,\text{momentum}}^{\text{aero}} + F_{22,\text{pressure}}^{\text{aero}}\right) \tag{3}$$

For the energy calculation, we assume a constant coefficient of isobaric specific heat (c_p) because ADflow does not have the necessary transport equations for chemical species. Under that assumption, we can derive the energy equation from the compressible integral conservation equations as

$$\Delta E_{\text{core}}^{\text{aero}} = c_p \left(\dot{m}_5^{\text{aero}} T_{t,5}^{\text{aero}} - \dot{m}_{22}^{\text{aero}} T_{t,22}^{\text{aero}}\right), \tag{4}$$

where c_p for air is $1.0045\,\text{kJ}/(\text{kg}\,\text{K})$. The momentum and energy change from the aerodynamic model are then passed to the BC coupling formulation in Eq. (10).

2.3 Propulsion Model

The propulsion system consists of two separate one-dimensional pyCycle [17] models for the core and fan that enable a mixed coupling strategy with the aerodynamic model. The fan is a compressor based on the NASA N+3 technology propulsion system [33] with a polytropic efficiency of 0.97. At both the fan face (station 2) and core face (station 22), we pass integrated values from the three-dimensional flow field to the one-dimensional models. Following best practices from Gray et al. [3] and Yildirim et al. [4], the inputs common to both propulsion models are *mass-averaged* velocity, *area-averaged* static pressure, mass flow rate, and area. The fan model receives a fan pressure ratio from the CFD model, computed as the fraction of *area-averaged* total pressures across the fan disk;

$$\mathrm{PR}_{\mathrm{fan}} = \frac{P_{t,13}^{\mathrm{aero}}}{P_{t,2}^{\mathrm{aero}}}. \tag{5}$$

Using turbomachinery maps, the fan computes the enthalpy rise across the standalone compressor based on the incoming flow properties and fan pressure ratio. We compute the heat addition ($\mathscr{P}_{\mathrm{heat}}$) as the difference between the ideal and real specific enthalpy at the fan exit, multiplied by the mass flow rate:

$$\mathscr{P}_{\mathrm{heat}} = \dot{m}_2^{\mathrm{aero}}(h_{\mathrm{ideal}}^{\mathrm{prop}} - h_{\mathrm{real}}^{\mathrm{prop}}) \tag{6}$$

This results in a fully coupled nonlinear system that includes the CFD and fan models, which is solved using a nonlinear solver, shown in Fig. 2. This analysis loop between the fan and the aerodynamic models are converged before we further analyze the core model.

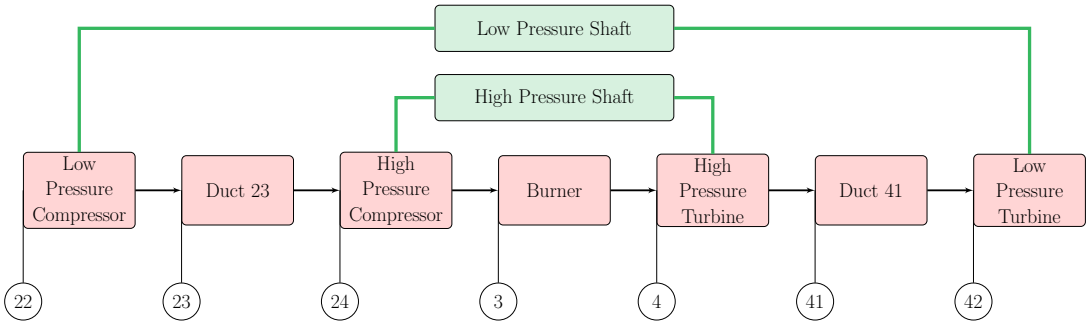

Figure 7 – Flow station numbering and element labels for the turbofan engine core model. This flow path is representative of a turbojet, where the red elements are part of the one-dimensional cycle and green signifies a mechanical element or connection. The black arrows show the direction of the flow through the core.

The one-dimensional core model, shown as a flow path diagram in Fig. 7, begins at the LPC inlet and ends with the LPT outflow. We specify several nonlinear implicit relationships called *balances* that enforce physical governing equations, conservations laws, and design rules. These balances are represented as residuals, shown in Eq. (7), that require a nonlinear solver to find the states (u) that result in zero residuals ($r(u) = 0$). We impose two design balances that vary the fuel-to-air ratio (FAR) and high pressure compressor pressure ratio ($\mathrm{PR}_{\mathrm{hpc}}$) to satisfy a design value of burner exit temperature ($T_{t,4}$) and overall pressure ratio (OPR), respectively. Next, two physical balances are added to balance the power ($\mathscr{P}$) on the low and high pressure shafts. The high pressure shaft residual drives the power needed by the HPC to be equal to the power generated by the HPT. On the low pressure spool, we balance the power requested by the fan and LPC with the power generated by the LPT. Since the fan is a separate model, we connect the torque (τ_{fan}) to the low pressure shaft in the core to ensure the balance accounts for the power needed by the fan. The residuals we define using the core model are listed as:

$$r_{\mathrm{core}}(u) \rightarrow \begin{cases} r(\mathrm{FAR}) &= T_{t,4} - T_{t,4,\mathrm{des}} = 0, \\ r(\mathrm{PR}_{\mathrm{hpc}}) &= \mathrm{OPR} - \mathrm{OPR}_{\mathrm{des}} = 0, \\ r(\mathrm{PR}_{\mathrm{lpt}}) &= \mathscr{P}_{\mathrm{LP,shaft}}^{\mathrm{in}} - \mathscr{P}_{\mathrm{LP,shaft}}^{\mathrm{out}} = 0, \\ r(\mathrm{PR}_{\mathrm{hpt}}) &= \mathscr{P}_{\mathrm{HP,shaft}}^{\mathrm{in}} - \mathscr{P}_{\mathrm{HP,shaft}}^{\mathrm{out}} = 0. \end{cases} \tag{7}$$

We complete the definition of the core model by specifying the inputs in Table 1. These inputs are chosen to represent current technology levels for the burner and turbomachinery components. With a converged design, we calculate the change in energy and momentum across the core using a one-dimensional control volume analysis, given in Eqs. (8) and (9) respectively. The change in energy and momentum are used in the BC coupling method in Eq. (10) and are outputs of the core model in Fig. 2.

$$\Delta E_{\text{core}}^{\text{prop}} = \dot{m}_5^{\text{prop}} h_{t,5}^{\text{prop}} - \dot{m}_{22}^{\text{prop}} h_{t,22}^{\text{prop}} \tag{8}$$

$$\Delta F_{\text{core}}^{\text{prop}} = (\dot{m}_5^{\text{prop}} V_5^{\text{prop}} + P_{s,5}^{\text{prop}} A_5^{\text{prop}}) - (\dot{m}_{22}^{\text{prop}} V_{22}^{\text{prop}} + P_{s,22}^{\text{prop}} A_{22}^{\text{prop}}) \tag{9}$$

2.4 Aeropropulsive Coupling

It is challenging to connect three-dimensional CFD analyses to one-dimensional cycle models because information is lost during the reduction in dimensionality. To make matters more complicated, the underlying thermodynamic models of the CFD solver ADflow and the cycle modeling tool pyCycle are not the same. Yildirim et al. [4] proposed the AZ and BC coupling strategies to overcome these challenges. The AZ method creates a cyclic loop between the aerodynamic and fan models that we converge using a nonlinear block Gauss-Seidel solver (NLBGS). The NLBGS solver operates on the cycle outlined by black arrows on the XDSM diagram in Fig. 2.

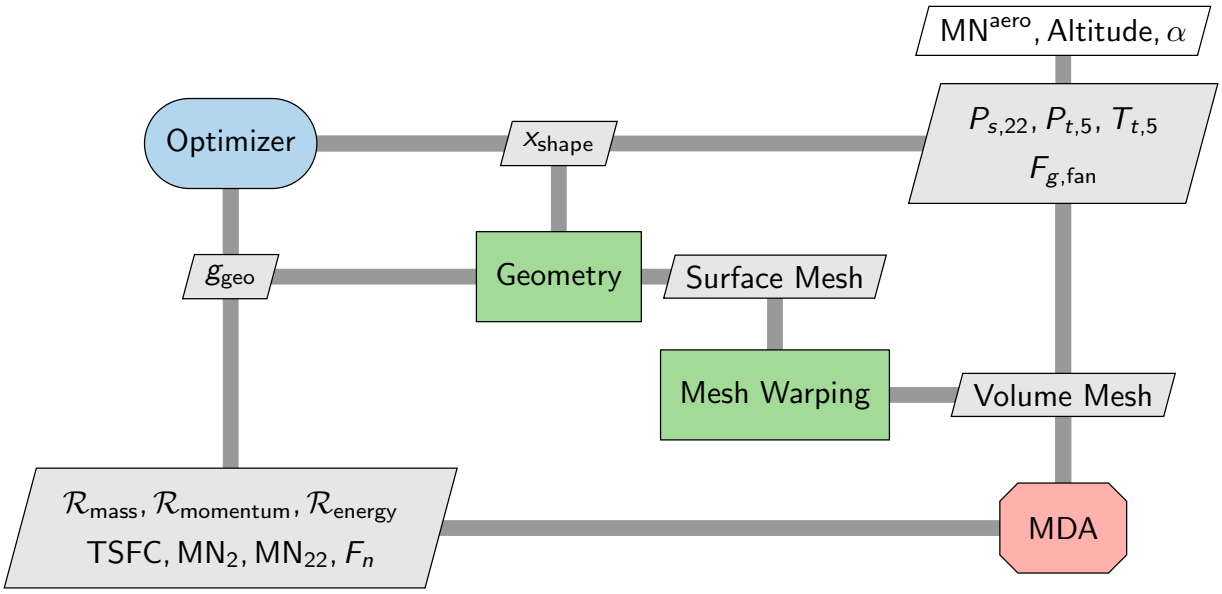

Figure 8 – XDSM diagram of the optimization framework. The outputs of the optimizer are the design variables and the output of the MDA and geometry blocks are the functions of interest.

We cannot readily design a flow through mesh for an engine core due to its size and complexity, thus we chose to use powered boundary conditions to couple the engine core to the CFD model. The BC approach stems from the compressible flow integral conservation equations applied to a control volume that encloses the engine core. We calculate the change in mass, momentum, and energy from both the pyCycle and ADflow models separately and use Eq. (10) to compute the difference

Table 1 – Core one-dimensional cycle inputs that specify the design of the turbomachinery and burner. The compressor and turbine efficiencies, OPR, and $T_{t,4}$ inputs are at current or near future technology readiness levels.

η_{lpc}	η_{hpc}	η_{lpt}	η_{hpt}	PR_{lpc}	$T_{t,4}$	OPR	$N_{\text{LP,shaft}}$	$N_{\text{HP,shaft}}$
92.43%	87.07%	89.96%	88.88%	1.935	2850.0 R°	25.0	4666.1 rpm	14,705.7 rpm

between the two models. The difference creates residuals that we pass to the optimizer as equality constraints.

$$\begin{aligned} \mathscr{R}_{\text{mass}} &= \dot{m}_{22}^{\text{aero}} + \dot{m}_{\text{fuel}}^{\text{prop}} - \dot{m}_{5}^{\text{aero}} = 0 \\ \mathscr{R}_{\text{momentum}} &= \Delta F_{\text{core}}^{\text{prop}} - \Delta F_{\text{core}}^{\text{aero}} = 0 \\ \mathscr{R}_{\text{energy}} &= \Delta E_{\text{core}}^{\text{prop}} - \Delta E_{\text{core}}^{\text{aero}} = 0 \end{aligned} \tag{10}$$

If the equality constraints are satisfied with a given design, we consider the design to be in a feasible design space. The caveat with this approach is that attaining a feasible design requires the use of an optimizer and every additional constraint constitutes an extra adjoint solution. Formulating the same coupling approach is also possible by satisfying the conservation equations using a nonlinear solver; however, this approach requires a fully coupled solver which requires significant development effort [4]. Therefore, we use equality constraints to satisfy these equations.

3. Optimization Problem Definition

The objective of the optimization problem is to minimize the thrust specific fuel consumption (TSFC) at a cruise flight condition subject to geometric, aerodynamic, and conservation constraints. We define the cruise condition at a Mach number of 0.78, altitude of 37,000 ft, and angle of attack of $0°$. The geometric toothpick constraints introduced in Section 2.1 place lower and upper bounds on the thickness of the nacelle and core as a substitute for structural considerations. We limit the fan and LPC face Mach number values to less than 0.6 and 0.45, respectively, to accommodate for compressor blade design parameters that are not considered in this analysis. Net thrust and fan diameter constraints of 5500 lbf and 81 inches, respectively, are enforced to drive the final result towards a physical thermodynamic and geometric design. Finally, the conservation constraints from the BC coupling method enforce continuity, momentum, and energy match across the one-dimensional cycle and aerodynamic models. The complete optimization problem formulation is listed in Table 2.

Table 2 – Single-point optimization problem definition. There are 20 shape design variables and 4 aerodynamic design variables. The objective function and seven constraints depend on the coupled aeropropulsive solution.

	Variable/Function	Description	Quantity
minimize	TSFC	Thrust specific fuel consumption	1
with respect to	$F_{g,\text{fan}}$	Force applied by the fan	1
	$P_{s,22}$	Static pressure at flow station 22	1
	$T_{t,5}$	Total temperature at flow station 5	1
	$P_{t,5}$	Total pressure at flow station 5	1
	x_{nacelle}	Nacelle shape	12
	x_{core}	Core shape	6
	x_{plug}	Plug shape	1
	x_{offset}	Duct21 offset	1
		Total	24
subject to	$F_n = F_n^*$	Target net thrust	1
	$\text{MN}_{\text{ff}} \leq 0.6$	Upper limit of fan face Mach number	1
	$\text{MN}_{22} \leq 0.45$	Upper limit of LPC face Mach number	1
	$\mathscr{R}_{\text{mass}} = 0$	Conservation of mass across the fan	1
	$\mathscr{R}_{\text{momentum}} = 0$	Conservation of momentum across the fan	1
	$\mathscr{R}_{\text{energy}} = 0$	Conservation of energy across the fan	1
	$0.99 \leq g_{\text{geo}} \leq 3.0$	Geometric thickness constraints	17
		Total	23

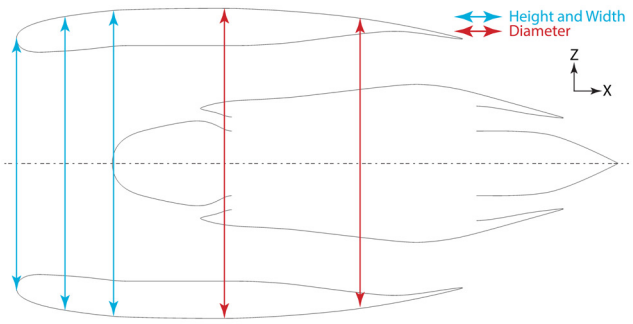

(a) Geometric design variables on the outer nacelle.

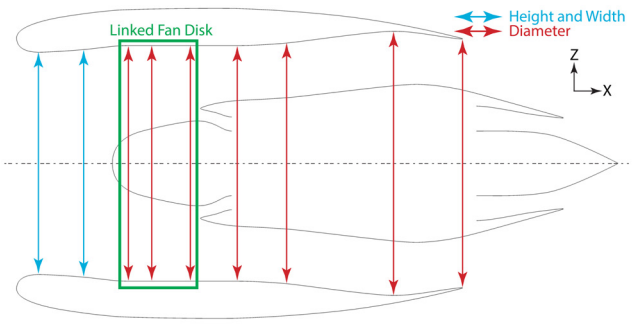

(b) Geometric design variables on the inner nacelle. The cross sections outlined in green are linked to represent a uniform diameter across the fan disk.

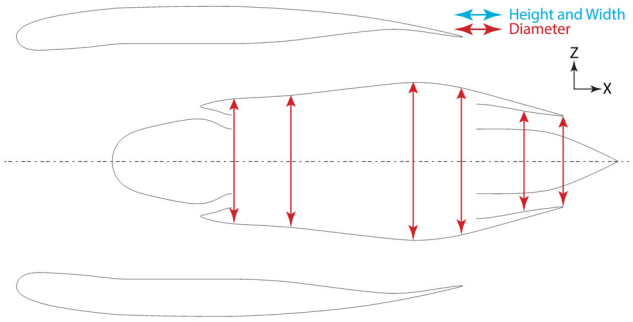

(c) Geometric design variables on the engine core.

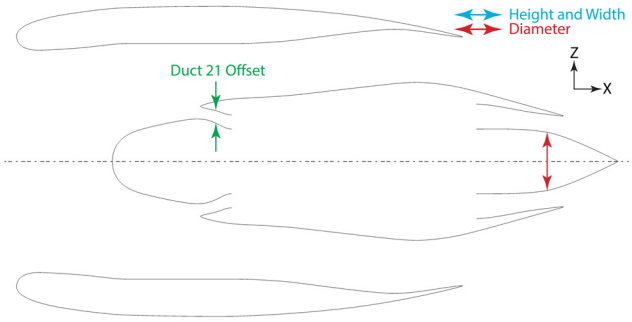

(d) Duct 21 offset design variable and the single cross section design variable on the core plug.

Figure 9 – Geometric shape design variables overlaid on a symmetric cross section of the turbofan model.

We chose design variables that give the optimizer adequate thermodynamic and geometric degrees of freedom to satisfy the constraints while adhering to typical engine design guidelines. Figure 9 shows the geometric shape design variables the optimizer can vary, written as x_{nacelle}, x_{core}, x_{plug}, and x_{offset} in Table 2. The thermodynamic design variables are fan thrust ($F_{g,\text{fan}}$), total pressure and temperature at station 5 ($P_{t,5}$, $T_{t,5}$), and the static pressure at station 22 ($P_{s,22}$).

The coupled aeropropulsive design optimization framework shown in Fig. 8 is developed using the MPhys library,[2] which is an open-source multiphysics simulation and optimization library built with the OpenMDAO framework [19]. The OpenMDAO framework uses the MAUD architecture to automatically solve the coupled derivative problem [34]. The MAUD architecture only requires the partial derivatives from each computational component to compute the total coupled derivatives. The ADflow partial derivatives are computed using algorithmic differentiation [30], the pyCycle partials are computed analytically [17], and we employ a parallel finite-differencing approach for the OpenVSP derivatives. We utilize the adjoint approach to compute the derivatives of the functions of interest with respect to the design variables since the number of functions of interest that rely on the coupled aerodynamic state is fewer than the number of design variables.

We solve the optimization problem using SNOPT [35], a gradient-based sequential quadratic programming (SQP) algorithm for large-scale constrained optimization. We access SNOPT using the python interface pyOptSparse [36], a framework for efficiently solving nonlinear constrained optimization problems.

4. Results

The goal of this work is to introduce a novel approach for mixed-fidelity propulsion system design using gradient-based optimization. The optimization problem from sec. 3.is solved with a net thrust

[2] https://github.com/OpenMDAO/mphys

constraint equal to 5500 lbf and an upper bound of 81 inches on the fan diameter. Since we do not vary the $T_{t,4}$ or OPR of the core cycle, these constraints place effective limits on the fan pressure ratio and bypass ratio (BPR). In conjunction with the Mach number and BC coupling constraints, the optimizer is able to find a feasible engine design. Figure 10 shows the feasibility and optimality achieved for this optimization problem. The feasibility converges below the requested tolerance of 10^{-4}, but the optimality struggles to improve further than 10^{-2} in 113 iterations. The optimization ran in 14 hours and 41 minutes on 30 Broadwell nodes with 28 core per node on the Pleiades supercomputer at the NASA Ames Research Center.

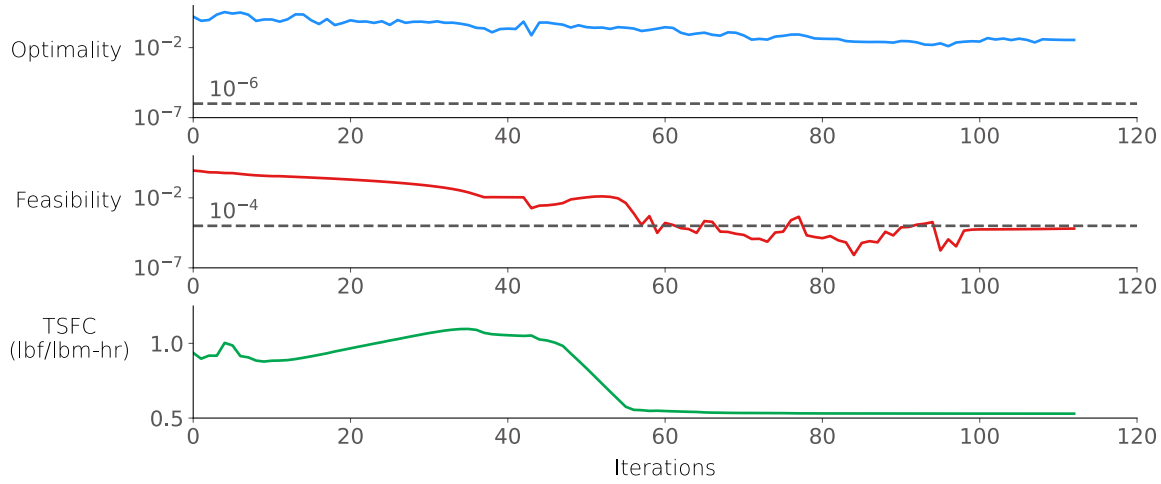

Figure 10 – The optimality and feasibility at each iteration for the coupled aeropropulsive optimization. The optimality does not reach the requested tolerance but the design is feasible and the objective function decreases significantly from the baseline design

We see in Figs. 11 and 13 the optimizer increases the net fan thrust and fan diameter to the upper bound, effectively maximizing the fan pressure ratio to meet the net thrust constraint. The larger fan pressure ratio increases the total pressure and mass flow rate in the bypass duct, which is followed by a decrease in the bypass nozzle area to maintain a choked throat and maximize thrust. Comparing Figs. 11 and 12, as the fan thrust goes up $P_{t,5}$ and $P_{s,22}$ also rise because the core mass flow rate and subsequently the momentum increase according to Eq. (9). However, as the bypass duct and nozzle approach a more optimal shape, $P_{t,5}$ and $P_{s,22}$ must decrease because less mass is being forced through the core.

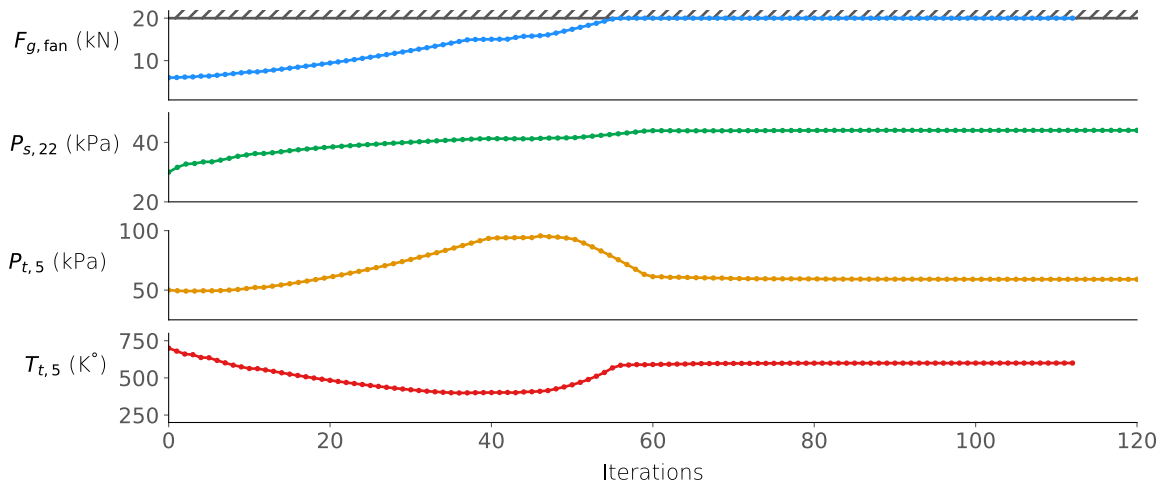

Figure 11 – Aerodynamic design variables plotted against optimization iterations. The net thrust increases to the upper bound to maximize the bypass ratio and fan pressure ratio. The optimizer varies the other three variables to satisfy the BC coupling constraints.

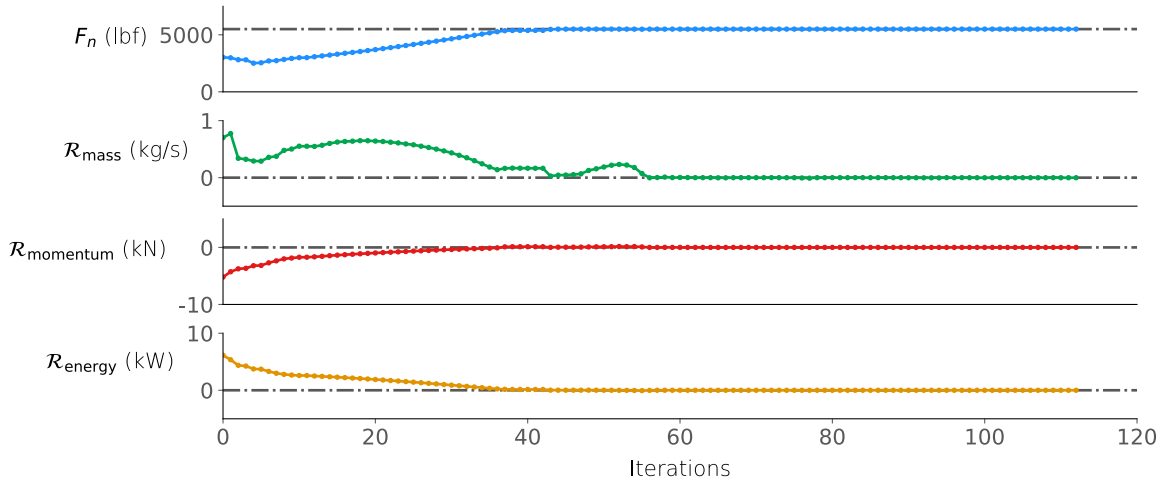

Figure 12 – The net thrust and BC coupling constraints plotted against optimization iterations. The three conservation residuals converge to zero which represents a balanced coupling formulation between the one-dimensional cycle and aerodynamic models.

As the fan thrust increases, the mass flow rate through the core decreases and the PR_{lpt} rises to sustain the necessary power on the low pressure shaft. A higher PR_{lpt} means more total enthalpy is lost across the low pressure turbine and subsequently the optimizer must decrease $T_{t,5}$ to satisfy the energy constraint. Once the bypass nozzle reaches a choked state for such a large fan thrust, the torque required to sustain the fan pressure ratio decreases, in turn causing the core energy and $T_{t,5}$ to increase.

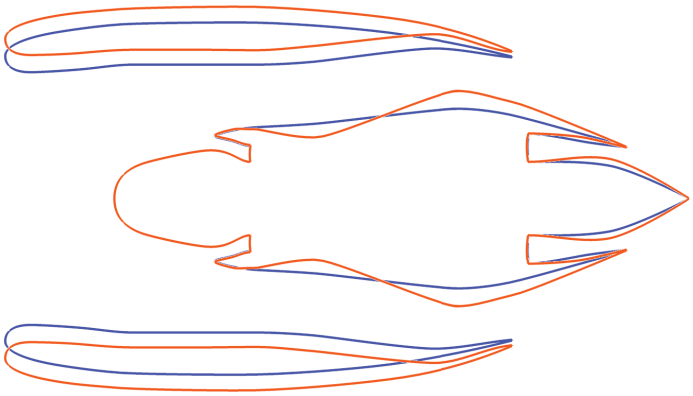

Figure 13 – The geometry of the solution (orange) overlaid on the baseline design (blue) along the symmetry plane. The solution geometry has a larger fan diameter and bypass ratio, as well as a converging diverging core nozzle.

Figure 14a is the Mach number contours of the feasible design. We observe sonic flow at both the bypass and core nozzles that signifies the solution reaches a choked flow state. The dark purple hue forward of the fan disk and in duct 21 indicates that the Mach number constraints are satisfied. In Fig. 14b, the AZ coupling is visible by the total pressure increase within the fan disk. The total pressure added at station 5 creates dark red contours at the outflow of the core nacelle, visualizing the increase in momentum generated by the core.

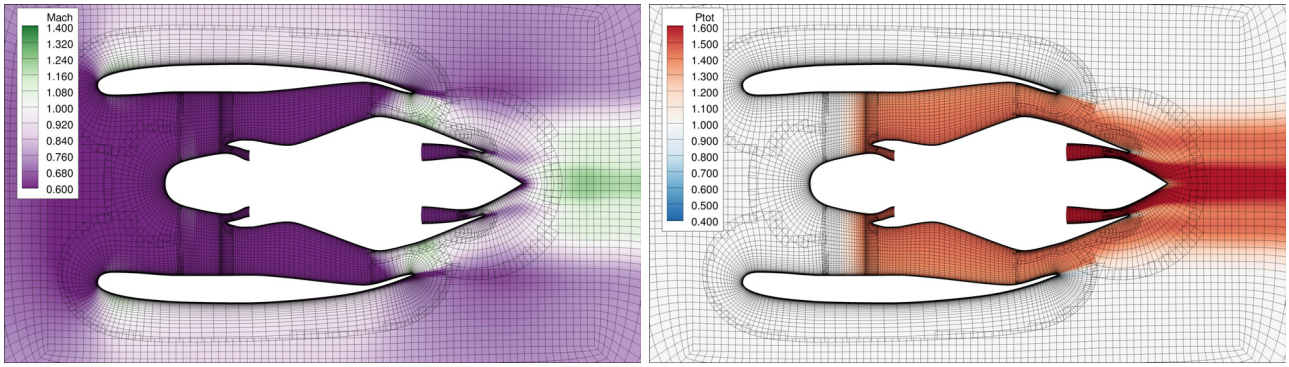

(a) Purple represents subsonic flow, white is sonic flow, and green is supersonic flow.

(b) The momentum added by the AZ is readily seen by the increase in total pressure in the fan disk. White is a normalized total pressure of one, where red is greater than one and blue is less than one.

Figure 14 – Mach number and total pressure contours for the feasible solution.

5. Conclusions

In this work, we introduced a mixed-fidelity and mixed-coupling approach to model and design advanced propulsion systems. We extended the methods developed by Gray et al. [3] and Yildirim et al. [4] to a tightly coupled turbofan configuration, where we use CFD to model the nacelle aerodynamics and two thermodynamic cycle models to model the fan and the engine core. These models are coupled together using both the AZ and BC coupling strategies for the fan and the engine core, respectively. We implemented the coupled model using the MPhys[3] library within the OpenMDAO framework [19], and applied the coupled adjoint method to compute derivatives of functions of interest with respect to design variables. The optimization problem minimizes TSFC subject to geometric, design, aerodynamic, and BC coupling constraints. Using a gradient-based optimizer, we successfully obtained a feasible design, where the three BC coupling constraints are satisfied.

This study represents a significant milestone in aeropropulsive design optimization capabilities. We introduced a coupled aeropropulsive model that captures the interactions between the nacelle aerodynamics and engine thermodynamics. This method, when combined with the availability of analytic derivatives, will speed up the design and integration of advanced aeropropulsive systems using gradient-based design optimization.

Acknowledgements

This work was supported by the U.S. Air Force Research Laboratory (AFRL) under the Michigan-AFRL Collaborative Center in Aerospace Vehicle Design (CCAVD), with Richard Snyder and Nathan Wukie as the task Technical Monitors.

6. Copyright Statement

[3] https://github.com/OpenMDAO/mphys

References

[1] Lytle, J. K., "Multi-fidelity simulations of air breathing propulsion systems," *Collection of Technical Papers - AIAA/ASME/SAE/ASEE 42nd Joint Propulsion Conference*, Vol. 8, No. July, 2006, pp. 6155–6161. doi:10.2514/6.2006-4967.

[2] Jones, S., *An Introduction to Thermodynamic Performance Analysis of Aircraft Gas Turbine Engine Cycles Using the Numerical Propulsion System Simulation Code*, NASA, 2007. TM-2007-214690.

[3] Gray, J., Mader, C. A., Kenway, G. K. W., , and Martins, J. R. R. A., "Approach to Modeling Boundary Layer Ingestion using a Fully Coupled Propulsion-RANS Model," *55th AIAA Aerospace Sciences Meeting (SciTech)*, Grapevine, TX, 2017. doi:10.2514/6.2017-1753.

[4] Yildirim, A., Gray, J. S., Mader, C. A., and Martins, J. R. R. A., "Coupled Aeropropulsive Design Optimization of a Podded Electric Propulsor," *AIAA Aviation Forum*, 2021. doi:10.2514/6.2021-3032.

[5] Kumano, T., Jeong, S., Obayashi, S., Ito, Y., Hatanaka, K., and Morino, H., "Multidisciplinary design optimization of wing shape with nacelle and pylon," *European Conference on Computational Fluid Dynamics*, 2006. URL `http://resolver.tudelft.nl/uuid:68c3395b-8045-4d27-b53f-71423ff9918f`.

[6] Albert, M., and Bestle, D., "Aerodynamic Design Optimization of Nacelle and Intake," 2013. doi:10.1115/GT2013-94857.

[7] Fang, X., Zhang, Y., Li, S., and Chen, H., "Transonic Nacelle Aerodynamic Optimization Based on Hybrid Genetic Algorithm," *17th AIAA/ISSMO Multidisciplinary Analysis and Optimization Conference*, American Institute of Aeronautics and Astronautics, 2016. doi:10.2514/6.2016-3833.

[8] Sasaki, D., and Nakahashi, K., "Aerodynamic Optimization of an Over-the-Wing-Nacelle-Mount Configuration," *Modelling and Simulation in Engineering*, Vol. 2011, 2011. doi:10.1155/2011/293078.

[9] Song, W., and Keane, A. J., "Surrogate-Based Aerodynamic Shape Optimization of a Civil Aircraft Engine Nacelle," *AIAA Journal*, Vol. 45, No. 10, 2007, pp. 2565–2574. doi:10.2514/1.30015.

[10] Savelyev, A., Zlenko, N., Matyash, E., Mikhaylov, S., and Shenkin, A., "Optimal Design and Installation of Ultra High Bypass Ratio Turbofan Nacelle," *Proceedings of the 18th International Conference on the Methods of Aerophysical Research*, Perm, Russia, 2016, p. 030123. doi:10.1063/1.4964065.

[11] Savelyev, A., Anisimov, K., Kazhan, E., Kursakov, I., and Lysenkov, A., "Computational Study of Engine External Aerodynamics as a Part of Multidisciplinary Optimization Procedure," *Proceedings of the 18th International Conference on the Methods of Aerophysical Research*, Perm, Russia, 2016, p. 020018. doi:10.1063/1.4963941.

[12] Bartoli, N., Lefebvre, T., Dubreuil, S., Panzeri, M., d'Ippolito, R., Anisimov, K., and Savelyev, A., "Robust Nacelle Optimization Design investigated in the AGILE European project," *2018 Multidisciplinary Analysis and Optimization Conference*, American Institute of Aeronautics and Astronautics, 2018. doi:10.2514/6.2018-3250.

[13] Lefebvre, T., Bartoli, N., Dubreuil, S., Panzeri, M., Lombardi, R., Vecchia, P. D., Stingo, L., Nicolosi, F., Marco, A. D., Ciampa, P., Anisimov, K., Savelyev, A., Mirzoyan, A., and Isyanov, A., "Enhancing optimization capabilities using the AGILE collaborative MDO framework with application to wing and nacelle design," *Progress in Aerospace Sciences*, Vol. 119, 2020, p. 100649. doi:10.1016/j.paerosci.2020.100649.

[14] Wang, Y., Shimada, K., and Farimani, A. B., "Airfoil GAN: Encoding and Synthesizing Airfoils for Aerodynamic-aware Shape Optimization," *arXiv preprint arXiv:2101.04757*, 2021.

[15] Lyu, Z., Xu, Z., and Martins, J. R. R. A., "Benchmarking Optimization Algorithms for Wing Aerodynamic Design Optimization," *Proceedings of the 8th International Conference on Computational Fluid Dynamics*, Chengdu, Sichuan, China, 2014. ICCFD8-2014-0203.

[16] Briones, A. M., Caswell, A. W., and Rankin, B. A., "Fully Coupled Turbojet Engine Computational Fluid Dynamics Simulations and Cycle Analyses Along the Equilibrium Running Line," *Journal of Engineering for Gas Turbines and Power*, Vol. 143, No. 6, 2021, p. 061019. doi:10.1115/1.4049410.

[17] Hendricks, E. S., and Gray, J. S., "pyCycle: A Tool for Efficient Optimization of Gas Turbine Engine Cycles," *Aerospace*, Vol. 6, No. 87, 2019. doi:10.3390/aerospace6080087.

[18] Mader, C. A., Kenway, G. K. W., Yildirim, A., and Martins, J. R. R. A., "ADflow: An open-source computational fluid dynamics solver for aerodynamic and multidisciplinary optimization," *Journal of Aerospace Information Systems*, Vol. 17, No. 9, 2020, pp. 508–527. doi:10.2514/1.I010796.

[19] Gray, J. S., Hwang, J. T., Martins, J. R. R. A., Moore, K. T., and Naylor, B. A., "OpenMDAO: An open-source framework for multidisciplinary design, analysis, and optimization," *Structural and Multidisciplinary Optimization*, Vol. 59, No. 4, 2019, pp. 1075–1104. doi:10.1007/s00158-019-02211-z.

[20] Hall, D. K., and Lieu, M., "Propulsor Models for Computational Analysis of Aircraft Aerodynamic Performance with Boundary Layer Ingestion," *Proceedings of the AIAA SciTech Forum*, American Institute of Aeronautics and Astronautics, 2021. doi:10.2514/6.2021-0991.

[21] Minaker, Q. J., and Defoe, J. J., "Prediction of Crosswind Separation Velocity for Fan and Nacelle Systems Using Body Force Models: Part 1: Fan Body Force Model Generation without Detailed Stage Geometry," *International Journal of Turbomachinery, Propulsion and Power*, Vol. 4, No. 4, 2019, p. 43. doi:10.3390/ijtpp4040043.

[22] Lambe, A. B., and Martins, J. R. R. A., "Extensions to the Design Structure Matrix for the Description of Multidisciplinary Design, Analysis, and Optimization Processes," *Structural and Multidisciplinary Optimization*, Vol. 46, 2012, pp. 273–284. doi:10.1007/s00158-012-0763-y.

[23] McDonald, R. A., "Interactive Reconstruction of 3D Models in the OpenVSP Parametric Geometry Tool," *53rd AIAA Aerospace Sciences Meeting*, American Institute of Aeronautics and Astronautics, 2015. doi:10.2514/6.2015-1014.

[24] Cumpsty, N., and Heyes, A., *Jet Propulsion: A Simple Guide to the Aerodynamics and Thermodynamic Design and Performance of Jet Engines*, 3rd ed., Cambridge University Press, 2015. doi:10.1017/CBO9781316223116.

[25] Yildirim, A., Gray, J. S., Mader, C. A., and Martins, J. R. R. A., "Aeropropulsive Design Optimization of a Boundary Layer Ingestion System," *AIAA Aviation Forum*, Dallas, TX, 2019. doi:10.2514/6.2019-3455.

[26] Yildirim, A., Mader, C. A., and Martins, J. R. R. A., "A Surface Mesh Deformation Method Near Component Intersections for High-Fidelity Design Optimization," *Engineering with Computers*, 2021. doi:10.1007/s00366-020-01247-w.

[27] Luke, E., Collins, E., and Blades, E., "A Fast Mesh Deformation Method Using Explicit Interpolation," *Journal of Computational Physics*, Vol. 231, No. 2, 2012, pp. 586–601. doi:10.1016/j.jcp.2011.09.021.

[28] Secco, N., Kenway, G. K. W., He, P., Mader, C. A., and Martins, J. R. R. A., "Efficient Mesh Generation and Deformation for Aerodynamic Shape Optimization," *AIAA Journal*, Vol. 59, No. 4, 2021, pp. 1151–1168. doi:10.2514/1.J059491.

[29] Spalart, P., and Allmaras, S., "A One-Equation Turbulence Model for Aerodynamic Flows," *La Recherche Aerospatiale*, Vol. 1, 1994, pp. 5–21.

[30] Kenway, G. K. W., Mader, C. A., He, P., and Martins, J. R. R. A., "Effective Adjoint Approaches for Computational Fluid Dynamics," *Progress in Aerospace Sciences*, Vol. 110, 2019, p. 100542. doi:10.1016/j.paerosci.2019.05.002.

[31] Yildirim, A., Kenway, G. K. W., Mader, C. A., and Martins, J. R. R. A., "A Jacobian-free approximate Newton–Krylov startup strategy for RANS simulations," *Journal of Computational Physics*, Vol. 397, 2019, p. 108741. doi:10.1016/j.jcp.2019.06.018.

[32] Hall, D. K., Greitzer, E. M., and Tan, C. S., "Analysis of Fan Stage Conceptual Design Attributes for Boundary Layer Ingestion," *Journal of Turbomachinery*, Vol. 139, No. 7, 2017, pp. 071012–071012–10. doi:10.1115/1.4035631.

[33] Jones, S. M., Haller, W. J., and Tong, M. T., "An N+3 Technology Level Reference Propulsion System," Tech. Rep. NASA/TM—2017-219501, NASA Glenn Research Center, 2017. URL `https://ntrs.nasa.gov/citations/20170005426`.

[34] Hwang, J. T., and Martins, J. R. R. A., "A computational architecture for coupling heterogeneous numerical models and computing coupled derivatives," *ACM Transactions on Mathematical Software*, Vol. 44, No. 4, 2018, p. Article 37. doi:10.1145/3182393.

[35] Gill, P. E., Murray, W., and Saunders, M. A., "SNOPT: An SQP algorithm for large-scale constrained optimization," *SIAM Journal of Optimization*, Vol. 12, No. 4, 2002, pp. 979–1006. doi:10.1137/S1052623499350013.

[36] Wu, N., Kenway, G., Mader, C. A., Jasa, J., and Martins, J. R. R. A., "pyOptSparse: A Python framework for large-scale constrained nonlinear optimization of sparse systems," *Journal of Open Source Software*, Vol. 5, No. 54, 2020, p. 2564. doi:10.21105/joss.02564.